Controlling Coherence Using the Internal Structure of Hard π Pulses

Yanqun Dong, R. G. Ramos, Dale Li, and S. E. Barrett*

Department of Physics, Yale University, New Haven, Connecticut 06511, USA†

(Received 18 April 2008; published 19 June 2008)

The tiny difference between hard π pulses and their delta-function approximation can be exploited to control coherence. Variants on the magic echo that work despite a large spread in resonance offsets are demonstrated using the zeroth- and first-order average Hamiltonian terms, for ^{13}C NMR in ^{60}C. The ^{29}Si NMR linewidth of silicon has been reduced by a factor of about 70 000 using this approach, which also has potential applications in magnetic resonance microscopy and imaging of solids.

DOI: 10.1103/PhysRevLett.100.247601 PACS numbers: 76.20.+q, 03.65.Yz, 76.60.Lz, 76.90.+d

In magnetic resonance, a control pulse is hard if the pulse amplitude is much greater than the spectral linewidth and any resonance offset; hard pulses are often approximated as instantaneous delta functions [1–3]. The corrections to this picture are quite small for a single hard pulse, but they can lead to surprisingly large effects [4,5] in important nuclear magnetic resonance (NMR) experiments that use many π pulses, such as the Carr-Purcell-Meiboom-Gill (CPMG) experiment [6,7]. CPMG uses a train of identical π pulses with the same phase that are equally spaced in time [1]. Despite this simple pattern of pulses, coherent averaging theory [8] shows that the zeroth- and first-order correction terms arising from nonzero pulse duration are quite complicated [4,5], making a quantitative prediction of their effects very difficult.

In this Letter, building upon our earlier results [4,5], we design more complicated pulse sequences and show that much simpler approximate Hamiltonians can quantitatively explain the experiments. This shows that the small difference between hard π pulses and their delta-function approximation can be put to good use, enabling new classes of spin echoes which have promising applications in NMR, magnetic resonance imaging (MRI) or MR microscopy of solids, and related spectroscopies.

The NMR data in Figs. 1–4 of this Letter were obtained with powder samples [C_{60} or silicon doped with Sb ($10^{17}/\mathrm{cm}^3$)] at room temperature, in $B_{\mathrm{ext}} = 12$ T. Both samples are well-approximated as a single species of spin $I = 1/2$ nuclei (^{13}C or ^{29}Si), coupled together by the like-spin dipolar interaction [4,5]. For a mesoscopic cluster of N spins, the Hamiltonian in the rotating frame is $\mathcal{H}_{\mathrm{int}} = \mathcal{H}_Z + \mathcal{H}_{zz}$, where a net resonance offset ($\Omega_z^{\mathrm{net}} = \Omega_{\mathrm{offset}}^{\mathrm{global}} + \Omega_z^{\mathrm{loc}}$) gives rise to the Zeeman term $\mathcal{H}_Z = \sum_i^N \Omega_z^{\mathrm{net}} I_{z_i} = \Omega_z^{\mathrm{net}} I_{z_T}$ and the secular part of the homonuclear dipolar coupling [1–3] is $\mathcal{H}_{zz} = \sum_{j>i}^N B_{ij}(3I_{z_i}I_{z_j} - \vec{I}_i \cdot \vec{I}_j)$. Our macroscopic powders are similar to an ensemble of N spin clusters, with distinct Ω_z^{loc} values in different clusters due to bulk diamagnetism [5]. The resulting Zeeman line broadening dominates the spectrum's full width at half maximum (FWHM), which was only about 2 ppm [e.g., the ^{13}C (^{29}Si) spectrum's measured FWHM = 260 (200) Hz, while the calculated dipolar FWHM = 38 (88) Hz]. The rf pulses used were unusually hard [e.g., the pulse strength $\omega_1/2\pi \approx 25$ (16.4) kHz was about 100 (82) times the ^{13}C (^{29}Si) linewidth, with a 128.56 (101.56) MHz Larmor frequency [1]]. Low coil filling factors [1] (<8% for ^{13}C data and ~40% for ^{29}Si data) made the rf pulses very uniform across the samples.

The open gray squares in Fig. 1(a) show the amplitude of each peak in a long-lived train of spin echoes [9] generated

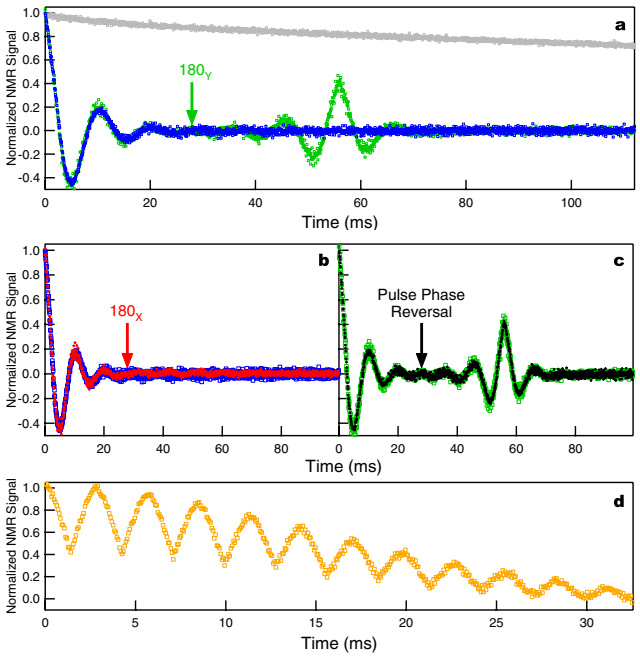

FIG. 1 (color online). Sample C_{60}. (a) Comparison of CPMG (gray) to APCPMG (blue). Inserting a single flip-180_Y pulse into APCPMG induces an echo of the echo train (green). (b) Inserting a single 180_X (red) has no effect (blue). (c) Reversing the APCPMG phase pattern $90_X - \{-Y, Y\}^{200} - \{Y, -Y\}^{600}$ at the point indicated has the same effect (black) as inserting a single 180_Y pulse (green). (d) A CPMG of the echo train is induced by using $90_X - \{-Y, Y\}^{10} - (\{Y, -Y\}^{20} - \{-Y, Y\}^{20})_{\mathrm{repeat}}$. For (a)–(d), $\tau = 25$ μs, $\Omega_{\mathrm{offset}}^{\mathrm{global}} = 0$, $\alpha \approx 0.71$, and only the peak of each echo is shown. The signals in Figs. 1–4 are normalized to the amplitude of the C_{60} or Si:Sb FID signal.

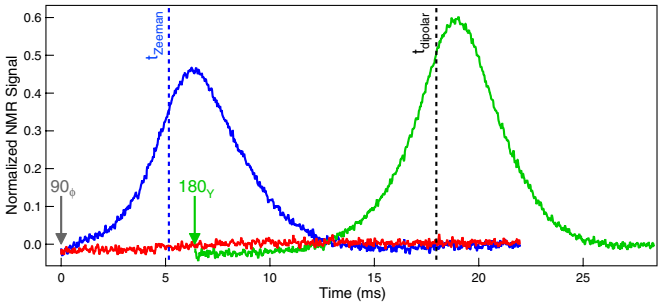

FIG. 2 (color online). Sample C_{60}. Three experiments inspired by the magic echo [10,11], which all start with $\{-X, X\}^N$, have distinctly different results. With 90_{-X} following the repeating block, no magic echo forms (red); with 90_{+X} following the repeating block, a large echo emerges (blue); when applying a 180_Y pulse at time t_{f_1} after the burst of the failed sequence (red), an optimized echo is achieved (green). Here $N = 200$, $\tau = 50\ \mu$s, $\Omega^{\text{global}}_{\text{offset}} = 0$, and $\alpha \approx 0.83$.

by the CPMG experiment $90_X - \{Y, Y\}^N$, where the first pulse is a 90° rotation about the X axis in the rotating frame [6,7]. The block $\{Y, Y\}$, repeated N times, represents the sequence $(\tau - 180_Y - 2\tau - 180_Y - \tau)$, where the 180° rotations are about the Y axis, and echoes are acquired in the 2τ time interval after every 180° (or π) pulse [1–3]. In contrast, the train of spin echoes quickly decays to zero [Fig. 1(a), blue] for alternating-phase CPMG (APCPMG) $90_X - \{-Y, Y\}^N$.

To understand this dramatic difference, we apply coherent averaging theory [8] to the repeating block $\{\phi_1, \phi_2\}$, with 180° pulses of duration t_p about the ϕ_1 or ϕ_2 axis and cycle time $t_c = 4\tau + 2t_p$. Short t_c is used throughout this Letter, so it is a good approximation to keep just the first two terms $\bar{\mathcal{H}}^{(0)} + \bar{\mathcal{H}}^{(1)}$ in the Magnus expansion [5]. The $\{Y, Y\}$ block has [5] $\bar{\mathcal{H}}^{(0)}_{\{Y,Y\}} = \alpha\mathcal{H}_{zz} - \beta\mathcal{H}_{yy} \equiv H$, while the $\{-Y, Y\}$ block has a slightly different form: $\bar{\mathcal{H}}^{(0)}_{\{-Y,Y\}} = H - \lambda\Omega^{\text{net}}_z I_{x_T}$, where $\alpha = \frac{4\tau}{t_c}$, $\beta = \frac{t_p}{t_c}$, $\lambda = \frac{4t_p}{\pi t_c}$, and $\mathcal{H}_{\sigma\sigma} = \sum_{j>i}^{N} B_{ij}(3I_{\sigma_i}I_{\sigma_j} - \vec{I}_i \cdot \vec{I}_j)$ for $\sigma = x$, y, or z. The extra term $-\lambda\Omega^{\text{net}}_z I_{x_T}$ looks like a constant transverse field in the X direction, which, when acting alone, causes spins to nutate [1] in the Y-Z plane in a manner we define as clockwise (CW). Variation in Ω^{net}_z values across the macroscopic sample leads to a spread in precession angles that causes signal decay. In the well-known free induction decay (FID), $T_2^\star$ arises from a spread in Ω^{net}_z of the original Zeeman Hamiltonian. By analogy, the rapid decay of the spin echoes produced by $90_X - \{-Y, Y\}^N$ [Fig. 1(a), blue] can be thought of as an "FID of the echo train."

Attempting to undo this $T_2^\star$-like decay, we insert a single 180_Y pulse into the APCPMG sequence $90_X - \{-Y, Y\}^{N_1} - 180_Y - \{-Y, Y\}^{N_2}$, which produces a striking "echo of the echo train" [Fig. 1(a), green]. Although this looks like a conventional Hahn echo [9], the signal actually extends over more than 800 individual spin echo peaks. The dephasing caused by $-\lambda\Omega^{\text{net}}_z I_{x_T}$ (CW precession) during the $N_1 t_c$ is followed by counterclockwise (CCW) precession caused by $+\lambda\Omega^{\text{net}}_z I_{x_T}$, and this rephasing leads to the echo of the echo train when $N_2 = N_1$. When a single flip-180_X is used instead, no echo of the echo train [Fig. 1(b), red] is seen, as predicted by our model, because a perfect rotation along the X axis does not change the sign of the $-\lambda\Omega^{\text{net}}_z I_{x_T}$ term. On the other hand, the echo of the echo train [Fig. 1(c), black] is recovered if the flip-180_X is removed, and the phase pattern in the second repeating block is reversed from $\{-Y, Y\}$ to $\{Y, -Y\}$, since [5] $\bar{\mathcal{H}}^{(0)}_{\{Y,-Y\}} = H + \lambda\Omega^{\text{net}}_z I_{xT}$, compared to $\bar{\mathcal{H}}^{(0)}_{\{-Y,Y\}} = H - \lambda\Omega^{\text{net}}_z I_{xT}$. In Fig. 1(c), the phase reversal of 1200 hard π pulses yields a signal indistinguishable from that induced by the single flip-180_Y, as predicted by our model. In contrast to this model, taking the limit of delta-function pulses ($t_p \to 0$) would kill [4,5] the transverse field terms in $\bar{\mathcal{H}}^{(0)} + \bar{\mathcal{H}}^{(1)}$ exploited here and throughout the rest of the Letter. Figure 1(d) shows that the approach of Fig. 1(c) can be repeated, creating multiple echoes in the envelope of individual spin echo peaks or a "CPMG of the echo train." However, the signal does decay, since the sign of the term H is never reversed in Fig. 1. To beat this decay, we use an approach inspired by the magic echo [1,10,11].

In the original magic echo [10–12], a continuous rf field in the transverse plane picks out the part of the dipolar coupling that is secular in the strong transverse field [1]. In the $\{-X, X\}$ block [5], the effective field $\lambda\Omega^{\text{net}}_z I_{y_T}$ in $\mathcal{H}^{(0)}_{\{-X,X\}}$ could play the same role, as first proposed by Pines and Waugh [13] for a single value of Ω^{net}_z. Figure 2 provides experimental support for their prediction, even though the weakness of the effective transverse field makes it hard to justify the second averaging analysis [13,14]. In addition, the spread in Ω^{net}_z across the macroscopic sample has nontrivial consequences, as shown by the different effects (Fig. 2) of the two bursts, $\{-X, X\}^N - 90_{\pm X}$, followed by a free evolution of duration t_{free}. Using our model, the unitary operators are $e^{-(i/\hbar)(\mathcal{H}_{zz}+\Omega^{\text{net}}_z I_{zT})t_{\text{free}}} e^{-(i/\hbar)(\frac{-(\alpha-\beta)}{2}\mathcal{H}_{zz} \mp \lambda\Omega^{\text{net}}_z I_{zT})Nt_c}\mathcal{U}_{90_{\pm X}}$, where $\pm X$ is the 90° pulse phase and $\alpha > \beta$ for our experiments [15].

For the $-X$ choice, the Zeeman phase wraps in a CCW manner both during and after the burst, which spoils the magic echo that would otherwise form during the free evolution period (Fig. 2, red). For the $+X$ choice, both Zeeman and dipolar terms switch from CW phase wrapping in the burst to CCW phase unwrapping during the free evolution period, resulting in a large echo (Fig. 2, blue). This echo is not optimized, since the refocusing time is different for the dipolar and Zeeman phases [$t_{\text{dipolar}} = (\alpha - \beta)Nt_c/2$, $t_{\text{Zeeman}} = \lambda Nt_c$]. An optimized echo (Fig. 2, green) is generated if we apply a 180_Y at time $t_{f_1} = (\frac{\alpha-\beta-2\lambda}{4})Nt_c$ after the failed sequence $\{-X, X\}^N - 90_{-X}$ (Fig. 2, red). This sequence aims to synchronize the refocusing times of the dipolar and Zeeman phases by using the

fact that a 180_Y pulse flips the sign of the Zeeman term but does not change the dipolar term. The measured echo happens at a slightly different time, due to terms ignored in this model [15].

Compared to the original magic echo [10,11], which works best if $\Omega_z^{\text{net}} = 0$, sequences based on the $\{-X, X\}^N$ block have several clear differences: Both Zeeman and dipolar phases are wrapped during the burst, a $90_{\pm X}$ is used instead of the 90_Y, and the 2τ gaps in between the π pulses of the $\{-X, X\}$ block simplify implementation.

The $\{\phi_1, \phi_2\}$ blocks used so far have an effective transverse field term in $\bar{\mathcal{H}}^{(0)}_{\{\phi_1,\phi_2\}}$. However, for the block $\{X, X\}$, $\bar{\mathcal{H}}^{(0)}_{\{X,X\}} = \alpha\mathcal{H}_{zz} - \beta\mathcal{H}_{xx}$, and so the first transverse field term is in $\bar{\mathcal{H}}^{(1)}_{\{X,X\}} = -(\kappa\Omega_z)^2 I_{x_T} + \bar{\mathcal{H}}^{(1),\text{non}-I_{x_T}}_{\{X,X\}}$, where $\kappa^2 = t_p(8\tau + 2t_p)/(2t_c\hbar\pi)$ [5]. In principle, despite its smaller size, the quadratic transverse field term of $\bar{\mathcal{H}}^{(1)}_{\{X,X\}}$ could be exploited just like the linear transverse field term found in $\bar{\mathcal{H}}^{(0)}_{\{-X,X\}}$. In practice, however, $\{X, X\}^N$ is a poor nutation experiment, since $\bar{\mathcal{H}}^{(1),\text{non}-I_{x_T}}_{\{X,X\}}$ causes rapid signal decay. Inspired by the rotary echo experiment [16], we tried replacing $\{X, X\}^N$ with the composite block $\{X, X\}^{N/2}\{-X, -X\}^{N/2}$ because $\bar{\mathcal{H}}^{(0)}_{\{-X,-X\}} = \bar{\mathcal{H}}^{(0)}_{\{X,X\}}$ and $\bar{\mathcal{H}}^{(1)}_{\{-X,-X\}} = -\bar{\mathcal{H}}^{(1)}_{\{X,X\}}$ [5], and we managed to recover most of the original signal. We thus infer [15] that the net effect of $\{X, X\}^{N/2}$-$\{-X, -X\}^{N/2}$ is well-approximated by the much simpler unitary operator $e^{-(i/\hbar)[-(1/2)\mathcal{H}_{xx}+(\kappa\Omega_z^{\text{net},-})^2 I_{xT}](Nt_c/2)} \times e^{-(i/\hbar)[-(1/2)\mathcal{H}_{xx}-(\kappa\Omega_z^{\text{net},+})^2 I_{xT}](Nt_c/2)}$, where we allow for different $\Omega_z^{\text{net},\pm}$ during $\{\pm X, \pm X\}^{N/2}$.

To test our model, we use phase-coherent frequency jumping $\Omega_z^{\text{net},\pm} = \Omega_z^{\text{loc}} \pm \Omega_{\text{offset}}^{\text{global}}$ $(\Omega_{\text{offset}}^{\text{global}} \geq 0)$ during the burst $\{X, X\}^{N/2}\{-X, -X\}^{N/2} - 90_Y$, followed by $\Omega_{\text{offset}}^{\text{global}} = 0$ during free evolution, leading to [15] the unitary operator $e^{-(i/\hbar)(\mathcal{H}_{zz}+\Omega_z^{\text{loc}} I_{zT})t_{\text{free}}} \times e^{-(i/\hbar)[-(1/2)\mathcal{H}_{zz}-(2\kappa^2\Omega_{\text{offset}}^{\text{global}})\Omega_z^{\text{loc}} I_{zT}]Nt_c}\mathcal{U}_{90_Y}$. Increasing $\Omega_{\text{offset}}^{\text{global}}$ increases the Zeeman dephasing during the burst, pushing the quadratic echo peak out to larger values of t_{free} (Fig. 3, green and black). The inset in Fig. 3 shows the strong agreement between the Zeeman refocusing time predicted by our model (black trend line) and the quadratic echo peak measured in our experiments over a range of $\Omega_{\text{offset}}^{\text{global}}$. In contrast, the corresponding linear sequence $\{-X, X\}^{N/2}$-$\{X, -X\}^{N/2} - 90_X$ has its largest signal just after the burst, for all $\Omega_{\text{offset}}^{\text{global}}$ (Fig. 3, blue and red), as predicted in our model [15].

Controlling both dipolar and Zeeman phase wrapping using $\bar{\mathcal{H}}^{(1)}_{\{\phi_1,\phi_2\}}$ is an unusual aspect of the quadratic echo. As one use of this, we designed a composite block with no net dipolar evolution over a duration of 6Δ, $(\Delta + \delta) - 90_{\psi_1} - \{X, X\}^{N/2}\{-X, -X\}^{N/2} - 90_{\psi_2} - (\Delta - \delta)$, which we refer to as $\{N, \delta, \psi_1, \psi_2\}$, with $\Delta = Nt_c/4$, $|\delta| \leq \Delta$, and $\psi_i = \pm Y$ for $i = 1, 2$. For constant Ω_z^{net}, the unitary operator is $\mathcal{U}_{180_Y} e^{-(i/\hbar)(\Omega_z^{\text{net}} I_{zT})(+2\delta)}$ for $\psi_1 = \psi_2$ and $e^{-(i/\hbar)(\Omega_z^{\text{net}} I_{zT})(+2\Delta)}$ for $\psi_1 \neq \psi_2$ [15]. While similar effective operators were previously demonstrated [17] using magic sandwich echoes for $\|\mathcal{H}_Z\| \ll \|\mathcal{H}_{zz}\|$, our approach works in the complementary regime $\|\mathcal{H}_Z\| \geq \|\mathcal{H}_{zz}\|$, where the scales are calculated using $\|A\|^2 \equiv \text{Tr}(A^\dagger A)$ [2,5]. In particular, the $\{N, \delta, \psi_1, \psi_2\}$ sequence is still effective even when there is a large spread in Ω_z^{net} values across the sample [15].

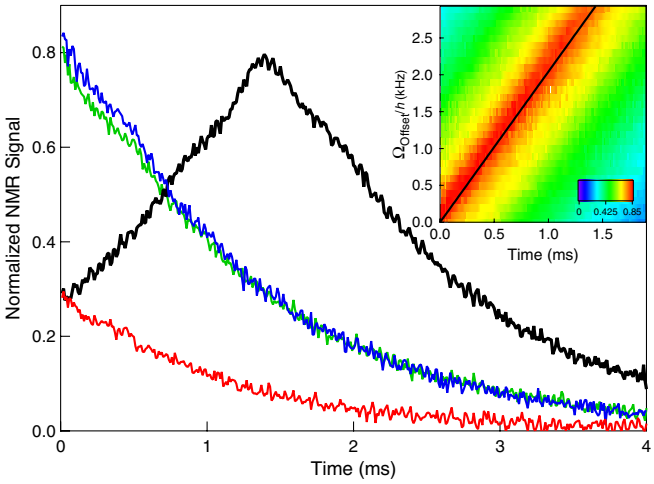

FIG. 3 (color online). Sample C_{60}. Using $\Omega_z^{\text{net},\pm} = \Omega_z^{\text{loc}} \pm \Omega_{\text{offset}}^{\text{global}}$, the quadratic echoes produced by $\{X, X\}^{N/2}$-$\{-X, -X\}^{N/2} - 90_Y - t_{\text{free}}$, green ($\nu_{\text{offset}} = 0$ Hz) and black ($\nu_{\text{offset}} = -3$ kHz), differ from the linear echoes produced by $\{-X, X\}^{N/2}\{X, -X\}^{N/2} - 90_X - t_{\text{free}}$, blue ($\nu_{\text{offset}} = 0$ Hz) and red ($\nu_{\text{offset}} = -1$ kHz), where $\Omega_{\text{offset}}^{\text{global}} = -h\nu_{\text{offset}}$. Only the black echo shifts to the right. Inset: Image plot of 31 quadratic echoes for $0 \text{ Hz} \leq \Omega_{\text{offset}}^{\text{global}}/h \leq 3$ kHz, in steps of 100 Hz. The black trend line shows our predicted Zeeman refocusing time. Here $N = 100$, $\tau = 10$ μs, and $\alpha \approx 0.5$.

Our model predicts that both Zeeman and dipolar phases are refocused after each $\{N, 0, \psi_1, \psi_1\}$ block, yielding a time-suspension sequence [17]. Indeed, in Si:Sb, our sequence pushes the decay time from $T_2^\star \approx 1.6$ ms out to $T_2^{\text{effective}} \approx 110$ s, or about 10^{10} periods of Larmor precession [Fig. 4(a), blue], quite close to the spin-lattice relaxation time $T_1 = 290$ s. The normal linewidth is thus reduced by a factor of about 70 000 [Fig. 4(a), inset].

Eliminating dipolar dephasing in order to measure Ω_z^{net} in applied magnetic field gradients enables the MRI [17–19] or MR microscopy [20] of solids. Measuring the spectrum in a field gradient is the first step toward imaging using the back-projection technique [1,19]. Figure 4(b) shows a faithful reproduction of an input top-hat spectrum, where each spectrum is the Fourier transformation of the pseudo-FID resulting from two interlaced data sets [15]. Note that both the signal amplitude and the ν_{offset} values have been quite accurately reconstructed in this approach. Compared to existing approaches for the MRI of solids [17–19], our approach does not need to switch off the applied Zeeman gradient inside the bursts, which enables

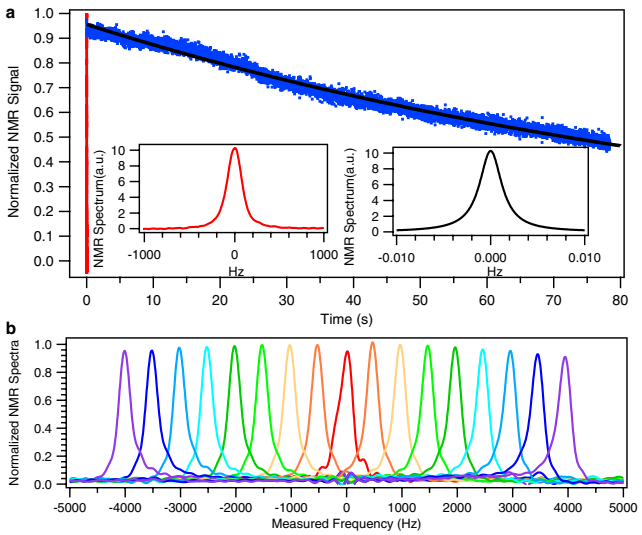

FIG. 4 (color online). (a) Sample Si:Sb. The ^{29}Si time-suspension data using the sequence $90_X - \{2, 0, -Y, -Y\}^{84\,000}$, with $\tau = 60$ μs, $\nu_{\text{offset}} = 2.5$ kHz (blue), and corresponding fitting curve (black), extend far beyond the normal ^{29}Si FID with $\nu_{\text{offset}} = 0$ Hz (red). (a, inset) The 200 Hz normal spectrum (red) is narrowed to 0.003 Hz (black, Fourier transformation of the fitting curve), centered at ν_{offset}. (b) Sample C_{60}. Reproduction of a top-hat line shape using sequence $90_X - \{2, t_0, -Y, -Y\} - \{2, 0, -Y, Y\}^{30}$, with $\tau = 22$ μs and $t_0 = 0$. Each trace is the measured spectrum of a pseudo-FID with different ν_{offset}, for -4 kHz $\leq \nu_{\text{offset}} \leq +4$ kHz in steps of 500 Hz, covering the range $2\pi|\nu_{\text{offset}}|/\omega_1 \leq 16\%$. To obtain this full bandwidth, the pseudo-FID interleaves a second data set using the same sequence but with $t_0 = -(\frac{\Delta}{2} + \frac{1}{2\omega_1})$.

the application of large field gradients at moderate cost. It should also be possible to implement standard frequency- and phase-encoding methods using this approach [1,19]. Since pulse strength varies across a big sample, the uniform pulse assumption of our model is a potential concern. Experimentally, an intentional uniform misadjustment of all pulse angles leads to similar MRI top-hat line shapes and to similar line-narrowing performance, suggesting that these two sequences are robust [15].

Our sequences may help in the study of some important biomaterials, since the $\mathcal{H}_{\text{int}}$ assumed here is very similar to that of ^{31}P in bones and teeth [21,22]. Preliminary results are encouraging [15]. These sequences also have potential applications in proton (^{1}H) NMR. While the dipolar line breadth dominates most ^{1}H spectra, a large $\Omega^{\text{global}}_{\text{offset}}$ can be used to reach the $\|\mathcal{H}_Z\| \geq \|\mathcal{H}_{zz}\|$ limit of our model, as demonstrated in our preliminary results on adamantane [15]. Future work will use microcoils [23–25] to reach shorter t_c, which should improve the utility of our model for proton NMR experiments.

Related effects can occur for a wider variety of $\mathcal{H}_{\text{int}}$ and $\mathcal{H}_{P_\phi}$ than we have treated here [5,15], provided that $[\mathcal{H}_{P_\phi}, \mathcal{H}_{\text{int}}] \neq 0$. Shaped pulses, soft pulses, and strongly modulated pulses have proven to be important elements of the NMR toolbox. Exploiting the internal structure of hard π pulses provides us with yet another technique to control the coherent evolution of quantum systems.

We thank K. W. Zilm, E. K. Paulson, and R. Tycko for discussions and thank M. H. Devoret, S. M. Girvin, A. Pines, and C. P. Slichter for comments on the manuscript. This work was supported by the NSF under Grants No. DMR-0207539, No. DMR-0325580, and No. DMR-0653377.

*sean.barrett@yale.edu
†http://opnmr.physics.yale.edu

[1] C. P. Slichter, *Principles of Magnetic Resonance* (Springer, New York, 1990), 3rd ed.
[2] M. Mehring, *Principles of High Resolution NMR in Solids* (Springer-Verlag, Berlin, 1983), 2nd ed.
[3] R. R. Ernst, G. Bodenhausen, and A. Wokaun, *Principles of Nuclear Magnetic Resonance in One and Two Dimensions* (Clarendon, Oxford, 1987).
[4] Dale Li, A. E. Dementyev, Yanqun Dong, R. G. Ramos, and S. E. Barrett, Phys. Rev. Lett. **98**, 190401 (2007).
[5] Dale Li, Yanqun Dong, R. G. Ramos, J. D. Murray, K. MacLean, A. E. Dementyev, and S. E. Barrett, arXiv:0704.3620 [Phys. Rev. B (to be published)].
[6] H. Y. Carr and E. M. Purcell, Phys. Rev. **94**, 630 (1954).
[7] S. Meiboom and D. Gill, Rev. Sci. Instrum. **29**, 688 (1958).
[8] U. Haeberlen and J. S. Waugh, Phys. Rev. **175**, 453 (1968).
[9] E. L. Hahn, Phys. Rev. **80**, 580 (1950).
[10] W. K. Rhim, A. Pines, and J. S. Waugh, Phys. Rev. Lett. **25**, 218 (1970).
[11] W. K. Rhim, A. Pines, and J. S. Waugh, Phys. Rev. B **3**, 684 (1971).
[12] K. Takegoshi and C. A. McDowell, Chem. Phys. Lett. **116**, 100 (1985).
[13] A. Pines and J. S. Waugh, J. Magn. Reson. **8**, 354 (1972).
[14] U. Haeberlen, J. D. Ellett, and J. S. Waugh, J. Chem. Phys. **55**, 53 (1971).
[15] R. G. Ramos, Yanqun Dong, Dale Li, and S. E. Barrett (to be published).
[16] I. Solomon, Phys. Rev. Lett. **2**, 301 (1959).
[17] S. Matsui, Chem. Phys. Lett. **179**, 187 (1991).
[18] J. B. Miller, D. G. Cory, and A. N. Garroway, Phil. Trans. R. Soc. A **333**, 413 (1990).
[19] D. E. Demco and B. Blumich, Concepts Magn. Reson. **12**, 269 (2000).
[20] P. Glover and P. Mansfield, Rep. Prog. Phys. **65**, 1489 (2002).
[21] Y. Wu, D. A. Chesler, M. J. Glimcher, L. Garrido, J. Wang, H. J. Jiang, and J. L. Ackerman, Proc. Natl. Acad. Sci. U.S.A. **96**, 1574 (1999).
[22] Y. Wu, J. L. Ackerman, H. M. Kim, C. Rey, A. Barroug, and M. J. Glimcher, J. Bone Miner. Res. **17**, 472 (2002).
[23] T. L. Peck, R. L. Magin, and P. C. Lauterbur, J. Magn. Reson., Ser. B **108**, 114 (1995).
[24] K. Yamauchi, J. W. G. Janssen, and A. P. M. Kentgens, J. Magn. Reson. **167**, 87 (2004).
[25] D. Sakellariou, G. Le Goff, and J. F. Jacquinot, Nature (London) **447**, 694 (2007).